A Model for the Structure of the Large-Pore Zeolite SSZ-31

Raul F. Lobo,*,† Michael Tsapatsis,*,§ Clemens C. Freyhardt,⊥,|| Ignatius Chan,‡ Cong-Yan Chen,‡ Stacey I. Zones,‡ and Mark E. Davis⊥

Contribution from the Center for Catalytic Science and Technology, Department of Chemical Engineering, University of Delaware, Newark, Delaware 19716, Department of Chemical Engineering, University of Massachusetts, Amherst, Massachusetts 01003, Division of Chemistry and Chemical Engineering, California Institute of Technology, Pasadena, California 91125, and Chevron Research and Technology Co., Richmond, California 94802

Received November 12, 1996[⊗]

Abstract: A model for the structure of the zeolite SSZ-31 is presented. The model is obtained by combining information from adsorption capacity measurements, transmission electron microscopy, and high-resolution X-ray diffraction. SSZ-31 is a one-dimensional large-pore zeolite with a framework density of 18.7 tetrahedral(T)-atoms per nm^{-3} and a bulk density of 1.87 g cm^{-3}. The pore apertures are elliptical with major and minor axes of approximately 8.6 Å × 5.7 Å. SSZ-31 is an extreme example of a complex and highly faulted zeolite. The structure can be described as an intergrowth of four different but structurally related polymorphs.

Introduction

The understanding of structure−property relations in zeolites and other microporous solids has been one of the keys to the successful industrial application of these materials.[1] Ideas concerning molecular sieving, shape-selective catalysis, the nature of the "active site", etc. are basic concepts used daily in catalysis and adsorption with zeolites that clearly depend on accurate and complete descriptions of the framework structures of these materials.[2,3] Hydrothermal, zeolite synthesis methods do not usually form materials amenable to direct structural analysis by single-crystal X-ray diffraction. The products are typically powders consisting of very small crystals (∼1 μm or less) that make structural characterization of these microporous solids a challenge.[4] Further complications often arise since many zeolites are disordered and/or present stacking faults that reduce the information that can be obtained from the X-ray powder diffraction pattern.[4] One well-known case of disorder due to frequent stacking faults is zeolite beta;[5,6] however, other instances of disorder in zeolites are common, including zeolites SSZ-26 and SSZ-33,[7,8] intergrowths of the FAU/EMT polytypes,[9] zeolite ZSM-48,[10] zeolite ZSM-12,[11] ZSM-11/ZSM-5,[12] etc.

The synthesis of SSZ-31 was first reported in 1991 using *N*,*N*,*N*-trimethyltricyclo[5.2.1.$0^{2,6}$]decaneammonium as the structure-directing agent.[13] Physicochemical data published previously suggest the existence of a one-dimensional large-pore system in the structure.[14] Additionally, Reddy et al. have previously shown that the zeolite NCL-1[15] and SSZ-31 show many similarities in their XRD patterns. Reddy et al. have also concluded that NCL-1 was possibly a one-dimensional large-pore zeolite.[15a]

We present here an investigation into the structure of the zeolite SSZ-31. This zeolite is an extreme example of the effect

* To whom correspondence should be addressed: Raul F. Lobo, Dept. of Chemical Engineering, University of Delaware, Newark, DE 19716. Off: (302) 831-8056, Fax: (302) 831-2085. e-mail: lobo@che.udel.edu. Michael Tsapatsis, Dept. of Chemical Engineering, University of Massachusetts, Amherst MA 01003. Off: (413) 545-0276. e-mail: tsapatsi@ecs.umass.edu.

† University of Delaware.

‡ Chevron Research and Technology Co.

§ University of Massachusetts.

⊥ California Institute of Technology.

|| Current address: Solid State Chemistry, Department of Chemistry, University of Constance, University Street 10, D-78434, Constance, Germany.

⊗ Abstract published in *Advance ACS Abstracts,* April 1, 1997.

(1) (a) Davis, M. E. *Chem. Ind.* **1992**, *4*, 137−139. (b) Moscou, L. *Stud. Surf. Sci. Catal.* **1991**, *58*, 1−12.

(2) (a) Santilli, D. S.; Zones, S. I. *Catal. Lett.* **1991**, *7*, 383−387. (b) Souverijns, W.; Rombouts, L.; Martens, J. A.; Jacobs, P. A. *Microporous Mater.* **1995**, *4*, 123−130.

(3) (a) Helmkamp, M. M.; Davis, M. E. *Ann. Rev. Mat. Sci.* **1995**, *25*, 161−192. (b) Lobo, R. F.; Zones, S. I.; Davis, M. E. *J. Inclusion Phenom. Mol. Recognit. Chem.* **1995**, *21*, 47−78. (c) Burkett, S. L.; Davis, M. E. *Chem. Mater.* **1995**, *7*, 1453−1463. (d) Behrens, P.; Van de Goor, G.; Freyhardt, C. C. *Angew. Chem., Int. Ed. Engl.* **1996,** *34*, 2680.

(4) (a) Baerlocher, C.; McCusker, L. B. *Stud. Surf. Sci. Catal.* **1994**, *85*, 391−428. (b) McCusker, L. *Acta Crystallogr. Sec. A* **1991**, *47*, 297.

(5) Higgins, J. B.; LaPierre, R. B.; Schlenker, J. L.; Rohrman, A. C.; Wood, J. D.; Kerr, G. T.; Rohrbaugh, W. J. *Zeolites* **1988**, *8*, 446−452.

(6) Newsam, J. M.; Treacy, M. M. J.; Koetsier, W. T.; de Gruyter, C. B. *Proc. R. Soc. London, Ser. A* **1988**, *420*, 375−405.

(7) (a) Lobo, R. F.; Pan, M.; Chan, I.; Li, H. X.; Medrud, R. C.; Zones, S. I.; Crozier, P. A.; Davis, M. E. *Science* **1993**, *262*, 1543−1546. (b) Lobo, R. F.; Pan, M.; Chan, I.; Medrud, R. C.; Zones, S. I.; Crozier, P. A.; Davis, M. E. *J. Phys. Chem.* **1994**, *98*, 12040−12052.

(8) Lobo, R. F.; Davis, M. E. *J. Am. Chem. Soc.* **1995**, *117*, 3766.

(9) (a) Treacy, M. M. J.; Vaughan, D. E. W.; Strohmaier, K. G.; Newsam, J. M. *Proc. R. Soc. London, Ser. A* **1996**, *452*, 813−840. (b) Arhancet, J. P.; Davis, M. E. *Chem. Mater.* **1991**, *3*, 567−569. (c) Anderson, M. W.; Pachis, K. S.; Previn, F.; Carr, S. W.; Terasaki, O.; Ohsuna, T.; Alfreddson, V. *J. Chem. Soc., Chem. Commun.* **1991**, 1660−1661.

(10) Schlenker, J. L.; Rohrbaugh, W. J.; Chu, P.; Valyosik E. W.; Kokotailo, G. T. *Zeolites* **1985**, *5*, 355−358.

(11) (a) LaPierre, R. B.; Rohrman, A. C.; Schlenker, J. L.; Wood, J. D.; Rubin, M. K.; Rohrbaugh, W. J. *Zeolites* **1985**, *5*, 346. (b) Fyfe, C. A.; Gies, H.; Kokotailo, G. T.; Marler, B.; Cox, D. E. *J. Phys. Chem.* **1990**, *94*, 3718.

(12) (a) Terasaki, O.; Ohsuna, T.; Sakuma, H.; Watanabe, D.; Nakagawa, Y. *Chem. Mater.* **1996**, *12*, 463. (b) Millward, G. R.; Ramdas, S.; Thomas, J. M.; Barlow, M. T. *J. Chem. Soc., Faraday Trans.* **1983**, *79*, 1075−1082.

(13) Zones, S. I. Harris, T. V.; Rainis, A.; Santilli, D. S. U.S. Patent 5 106 801 (1992).

(14) (a) Nakagawa, Y. *Stud. Surf. Sci. Catal.* **1994**, *84*, 323−330. (b) Nakagawa, Y.; Zones, S. I. In *Synthesis of Microporous Materials*; Occelli, M. L., Robson, H. E., Eds.; Van Nostrand Reinhold: New York, 1992; Vol. 1, p 222. (c) Zones, S. I.; Nakagawa, Y. *Microporous Mater.* **1994**, *2*, 543−555. (d) Nakagawa, Y. *Stud. Surf. Sci. Catal.* **1995**, *97*, 53−60. (b) Zones, S. I.; Nakagawa, Y. *Stud. Surf. Sci. Catal.* **1995**, *97*, 45−52.

(15) (a) Reddy, K. R.; Ramaswamy, V.; Kumar, R.; Ramaswamy, A. V. *Zeolites* **1994**, *14*, 326−334. (b) Ratnasamy, P.; Kumar, R. *Stud. Surf. Sci. Catal.* **1995**, *97*, 367−376. (c) Sasidharan, M.; Reddy, K. R.; Kumar, R. *J. Catal.* **1995**, *154*, 216−221. (d) Rao, P. R. H. P.; Reddy, K. R.; Ramaswamy, A. V.; Ratnasamy, P. *Stud. Surf. Sci. Catal.* **1993**, *78*, 385−392. (e) Reddy, K. R.; Ramaswamy, A. V.; Ratnasamy, P. *J. Chem. Soc., Faraday Trans.* **1992**, *21*, 1613−1615.

S0002-7863(96)03925-X CCC: $14.00

that stacking faults, disorder, and crystal size can have on the X-ray powder diffraction (XRD) pattern. The solution of the structure involved extensive characterization using electron diffraction, high-resolution electron microscopy, model building, and simulation of X-ray powder diffraction patterns using the program DIFFaX.[16] SSZ-31 is a one-dimensional large-pore zeolite that can be described as an intergrowth of four different but structurally related polymorphs. The structure of SSZ-31 is also important because of its relation to other high-silica zeolites, including zeolite beta, ZSM-12, UTD-1, ZSM-48, and SSZ-24. When synthesized with a small concentration of aluminum, SSZ-31 has already been shown to be a good solid-acid catalyst.[13]

Experimental Section

Material Synthesis. The syntheses of SSZ-31 are carried out under hydrothermal conditions using a gel of composition $1SiO_2$:0.15ROH:0.15NaOH:$45H_2O$ where R represents the structure-directing agent (see Supporting Information for a list of these molecules, details of the synthesis can be found elsewhere[17]). The samples were calcined in air at 923 K prior to analyses by XRD and electron microscopy.

Analytical. Synchrotron X-ray powder diffraction (XRD) data were obtained at the X7A beam line of the Synchrotron Light Source, Brookhaven National Laboratory. The sample was dried at 200 °C for 12 h and packed in a 1 mm glass capillary. The data were collected at room temperature from 2−65° 2Θ with a step scan of 0.01° and a wavelength, $\lambda = 1.1504$ Å. The results from the synchrotron data presented here have been modified to the corresponding 2Θ for a wavelength $\lambda = 1.54184$ Å (using Bragg's law) to facilitate comparison with the in-house XRD data. Room temperature powder X-ray diffraction patterns were recorded on a Scintag XDS 2000 diffractometer equipped with a liquid nitrogen germanium detector, $CuK_{\langle\alpha\rangle}$ radiation $\lambda = 1.54184$ Å and a Bragg-Brentano geometry using the step scan mode.

The adsorption capacities of SSZ-31, ZSM-5, zeolite Y, and zeolite ZSM-12 were measured at room temperature using a Cahn C-2000 balance coupled with a computer via an ATI-Cahn digital interface.[18] The adsorbate is delivered from the liquid phase, and the partial pressure P/P_0 is always maintained at less than 0.4. Prior to the adsorption experiments, the calcined zeolites are dehydrated at 615 K under a vacuum of 10^{-3} Torr for 5 h. The adsorption capacities are reported as milliliters of liquid per gram of dry zeolite.

The samples for transmission electron microscopy (TEM) are prepared by both direct-dispersion and microtomy. For direct-dispersion, a drop of the zeolite suspension in ethanol is transferred to a carbon-coated Cu-grid. For microtomy, the samples are first embedded in epoxy (LR white) by vacuum impregnation followed by heating at 90 °C for 2 h. Sections were prepared using a diamond knife mounted on an ultramicrotome. Thin sections were collected on a carbon coated Cu-grid. The sample grids are allowed to dry at 110 °C under vacuum overnight before mounting on the microscope specimen holder. Electron diffraction, transmission electron microscopy, and high-resolution electron microscopy (HREM) were performed on a Phillips 430 and JEOL 2000 CS microscopes operated at 200 KV. Image processing was carried out using the "Image" software for the MacIntosh.

Results and Discussion

SSZ-31 shows a characteristic X-ray powder diffraction pattern with mostly broad peaks. Figure 1 presents the XRD patterns of three samples of SSZ-31 prepared using three different structure directing agents. Typical morphologies of SSZ-31 crystals are shown in Figure 2. The predominant morphology is that of spherical and plate-like particles. These particles are mosaics consisting of aligned domains of ∼200 Å. In addition to the spherical particles, some elongated needles are present. Electron diffraction and structure imaging do not reveal structure differences between the two morphological types, and, therefore, no particular reference to the morphology is made in the following presentation.

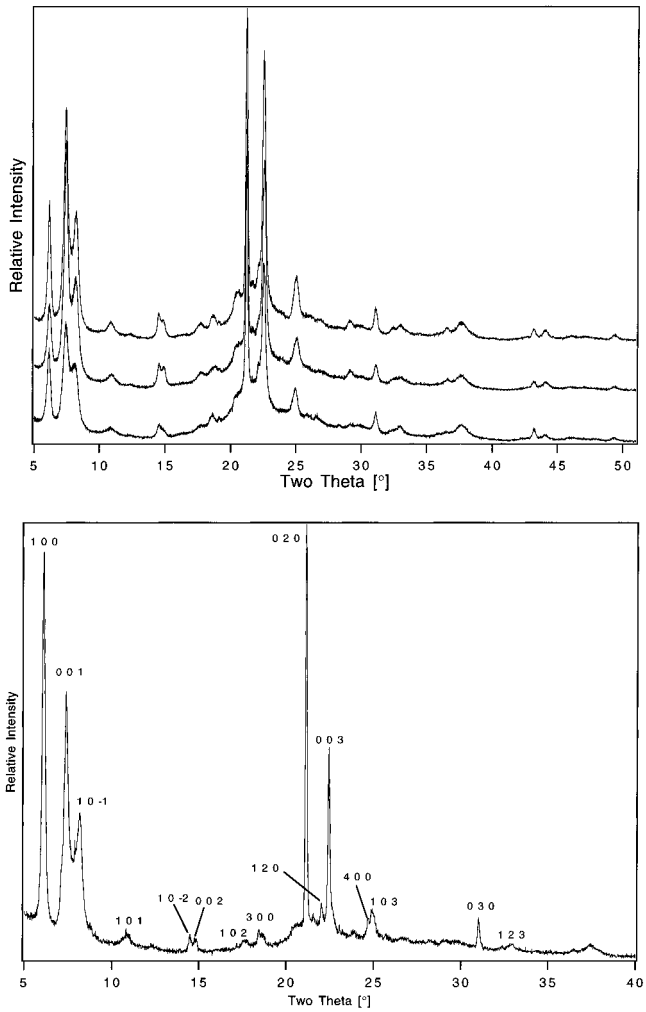

Figure 1. (a) X-ray powder diffraction patterns of three different samples of calcined SSZ-31 prepared using different structure-directing agents. (b) Synchrotron XRD pattern of SSZ-31 and the indexing of the most intense peaks according to the unit cell derived from electron diffraction.

The adsorption capacity of SSZ-31 is compared to the adsorption capacities of other zeolites in Table 1. It is clear that the adsorption capacity of SSZ-31 is very similar to that of SSZ-24 and ZSM-12, two large-pore one-dimensional molecular sieves. Comparison of the adsorption capacity of ZSM-5 and SSZ-31 shows that the diameter of the pores of SSZ-31 is larger than the diameter of the medium-pore zeolite ZSM-5, since 2,2-dimethylbutane does not adsorb to a significant extent in ZSM-5. Finally, the adsorption capacity of zeolite Y, a three-dimensional large-pore zeolite, is substantially higher than the adsorption capacity of SSZ-31. All of these data are in agreement with the hypothesis that SSZ-31 is a one-dimensional large-pore zeolite. These data are also consistent with the large sizes of the organic molecules used as structure-directing agents and with the chemical analysis that typically reveals a content of organic matter (C + N) near 10% w/w in the as-made material.

(16) Treacy, M. M. J.; Newsam, J. M.; Deem, M. W. *Proc. R. Soc. London, Ser. A* **1991**, *433*, 499−520. All the calculations have been carried out using v. 1.801 of the program using PPC Macintoch computer.

(17) Zones, S. I.; Nakagawa, Y.; Yuen, L. T.; Harris, T. V. *J. Am. Chem. Soc.* **1996**, *118*, 7558−7567.

(18) Lobo, R. F.; Chen, C. Y. et al. Manuscript in preparation.

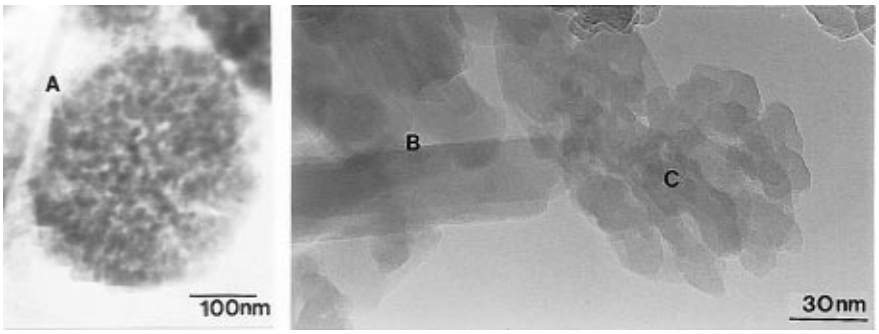

Figure 2. Typical morphologies of SSZ-31 particles. Spherical and plate-like mosaics (a, c) and elongated needles (b).

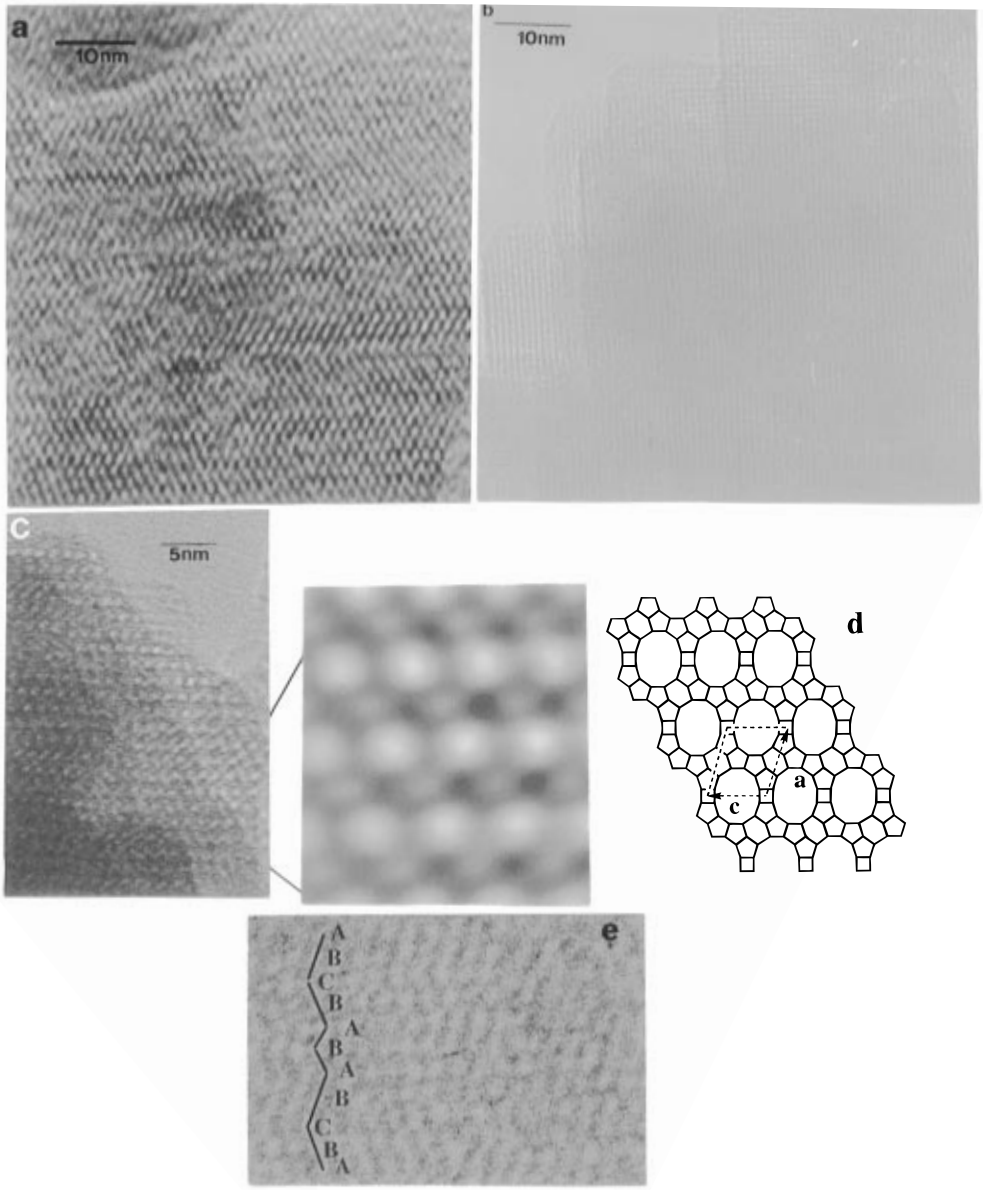

Figure 3. TEM view of SSZ-31 down (a) and perpendicular to the channels (b). An HREM view down the channels is showns in (c). The inset is a FFT filtered image of an ABC... sequence domain in the lower right part of (c). The 2-D net extracted from this image is shows in (d). A layer sequence in a faulted domain (e) illustrates the layer sequence in a faulted domain. An extended ABAB... sequence is shown, but this type of sequence is rare and ABC... type sequence is more common as shown in (a).

Transmission Electron Microscopy, Electron Diffraction, and HREM. Figure 3a shows a view down the zeolite channels, while Figure 3b shows a view perpendicular to the channels. Figure 3c is a structure image down the channels in which, in addition to the channel openings, six-membered rings can be resolved. From this image the two-dimensional net of SSZ-31 can be inferred (see below). These data confirm the presence of one-dimensional large-pores in SSZ-31.

Lattice images perpendicular to the channel direction (Figure 3b) are not sensitive to the precise orientation and usually exhibit a square or diamond array which follows in alignment the crystal edges. An analogous behavior has been observed by Newsam

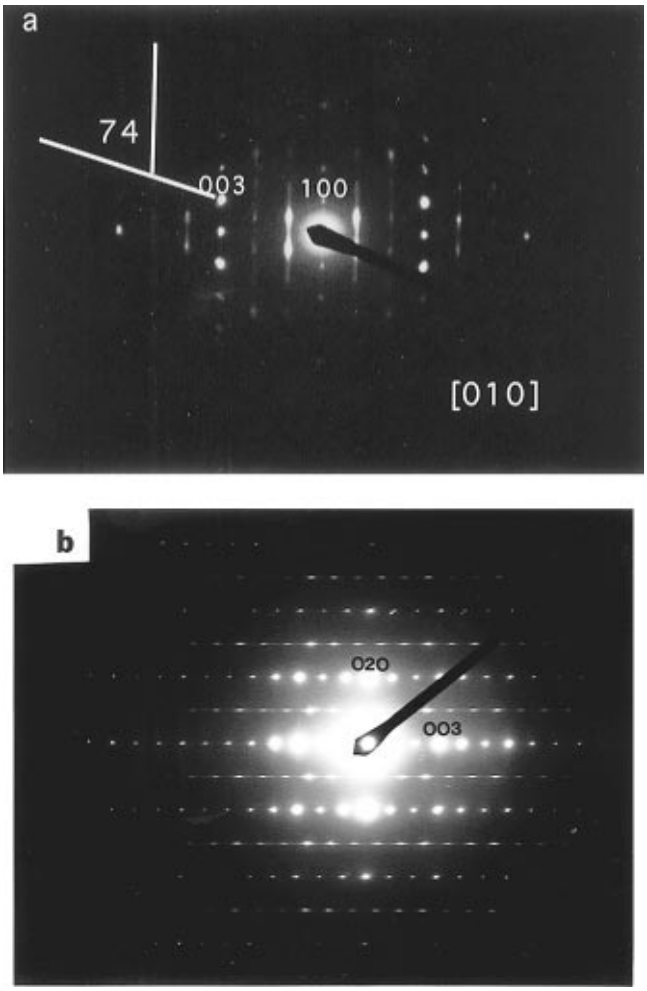

Figure 4. (a) Electron diffraction pattern along the [0 1 0] zone axis (view down the channels). (b) Electron diffraction pattern perpendicular to the channel direction [$\bar{1}$ 0 0] zone axis.

et al. for zeolite beta.[6] As will be discussed further below, this is due to the streaked reciprocal lattice as a result of stacking faults. Therefore, images like Figure 3b cannot provide useful structural information besides confirming the presence of stacking faults.

Figure 3a reveals the presence of stacking faults between planes of spacing ~14.4 Å. The stacking faults can be described (as was found for zeolite beta)[6] as interruption of the ABC... sequence by ABAB..., BCBC..., or CACA... sequences creating microtwins with both ABC... and CBA... sequences as shown in Figure 3e. Here A, B, and C are used to denote particular layers in the structure. The lateral displacement in the stacking of planes is approximately one-third of the lateral repeat distance (one-third of c where $c = 12.3$ Å). Analysis of several TEM pictures like Figure 3a show that more extended sections of ABC... or CBA... sequences dominate the ABAB... type of sequences. The presence of domains with extended ABC... sequences allows for image processing from such areas—the inset in Figure 3c shows a Fourier filtered image. A 2-D net can be extracted from this image as shown in Figure 3d.

An electron diffraction pattern along the [0 1 0] zone axis (view down the channels) is shown in Figure 4a. Streaking is observed in the first and second columns but not in the zeroth and third columns. The spot separations along the zeroth column correspond to the 14.4 Å layer spacing, while the distance between the columns corresponds to the 12.3 Å lateral repeat distance. A line drawn through the intensity maxima of the −third and third columns passing through the origin forming an angle of 74° (or 106°) with the zeroth order column is noted in the figure. The reflection on the third column that falls on this line corresponds to a spacing of 3.95 Å which would give a corresponding spacing for the spot in the first streaked column of 11.9 Å (3 × 3.95 Å). However, the intensity maximum in the streaked column is shifted from the 74° line due to the effect of the stacking faults. The electron diffraction pattern shown in Figure 4a is consistent with Figure 3a and confirms the presence of stacking faults between the layers of spacing 14.4 Å.

After analyzing these data, images like the one shown in Figure 3b can be interpreted as views perpendicular or nearly perpendicular to the fault planes. Since the reciprocal space is streaked along this direction, the Ewald sphere construction will intercept, in addition to Bragg reflections, streaked lines forming a diffraction pattern and/or a structure image exhibiting higher symmetry and being insensitive to tilting.

Figure 4b is an electron diffraction pattern with zone axes perpendicular to the channel direction. In this pattern, alternating rows of sharp and streaked spots are evident; the spacing between these rows being 8.4 Å. The spacing between the spots along the direction of the streaking in Figure 4b is 11.9 Å, which coincides with the spacing of the spots along the 74° line of Figure 4a. This observation verifies that the direction with the 8.4 Å repeat is perpendicular to the directions with repeat distances of 11.9 and 14.4 Å and thus is along the channel direction. These diffraction data, taken in total, lead to a preliminary assignment of a monoclinic unit cell with $a = 14.98$ Å, $b = 8.4$ Å, $c = 12.3$ Å, and $\beta = 106°$. The 11.9 Å spacing corresponds to the (0 0 1) planes.

In addition to the faulting between the planes with 14.4 Å spacing, Figure 4b reveals the presence of faulting or disorder in the perpendicular direction along the *b*-axis which involves translations of $^1/_2b$. The streaking in Figure 4b suggests that the faulting or disorder along the *b* direction can be described as taking place within the (1 0 0) planes. Diffraction patterns are often observed with streaking along two directions. The angle between the two directions along the streaking is 61° due to the faulting or disorder within the (1 0 0) and (0 0 1) planes.

X-ray Powder Diffraction Data. The X-ray powder diffraction patterns of three different samples of calcined SSZ-31 (Figure 1a) are representative of the differences in peak broadening and relative intensity that are often observed for different syntheses. All these samples have been prepared under similar reaction conditions, using only silica as the source of tetrahedral (T) framework atoms but using different structure-directing agents. Typically, most diffraction peaks are broad, and there is a relatively low signal-to-noise ratio. The height and width of certain diffraction peaks are sample dependent (specially at low 2Θ), an indication of differences in crystal morphology and size amongst different samples. The peak broadening is also due to the presence of stacking faults and/or other types of disorder in the zeolite structure as shown in the ED and HREM data above. Due to the broad XRD peaks, it is difficult to index these patterns accurately. Based on the results from the ED analyses, the presence of peaks at $d = 4.19$ Å, $d = 2.79$ Å, and $d = 2.09$ Å (2Θ = 21.2°, 32.1°, and 43.3°, respectively) can be assigned to the *0 2 0*, *0 3 0*, and *0 4 0* diffraction peaks and are in agreement with a unit cell axis of $b \sim 8.38$ Å (all the unit cell parameters are approximate within the limits of the technique). The first peak of the XRD patterns is at $d \sim 14.4$ Å (2Θ = 6.14°), and the second peak is at $d \sim 11.85$ Å (2Θ = 7.45°). These two peaks can be indexed as the *1 0 0* and the *0 0 1* reflections based on a monoclinic unit cell with an angle of $\beta = 106°$ and unit cell dimensions tentatively

estimated as $a = 14.98$ Å and $c = 12.33$ Å, in agreement with the ED results. Figure 1b shows the synchrotron XRD pattern with the preliminary indexing of the most intense diffraction peaks. Unequivocal indexing of the diffraction peaks of SSZ-31 cannot be accomplished because of the heavy stacking faults present in the material. This indexing is only tentative, and it is used below to develop possible frameworks that can be used as a basis for the simulation of disordered structures.

Because of the unusual characteristics of SSZ-31, we have used a nonstandard process for the characterization of the structure. This strategy starts from a two-dimensional three-connected model obtained from electron microscopy and the structural similarities of SSZ-31 to other zeolites. We use this model as the starting point to develop a set of possible frameworks. It will turn out that SSZ-31 contains two types of disorder. One type is similar to the disorder observed in zeolite beta, with heavy stacking faults. The second type of structural disorder is similar to the one observed in zeolite ZSM-48 in which, because all T-atoms are in two different conformations (up or down), many possible frameworks are consistent with the unit cell dimensions. In SSZ-31, it is possible to form at least 63 frameworks consistent with a monoclinic polymorph and 63 consistent with an orthorhombic polymorph. All these models have the same framework density, pore dimensions, and projected potential along the pore direction: these data cannot be used to distinguish between the different frameworks. Also, because of the faulting, we would have to analyze simulations of the X-ray diffraction patterns of intergrowths of 3969 combinations—that is, assuming the structure is a mixture of only two pure polymorphs—to identify the one combination with the best fit to the data. To simplify this task, a series of empirical criteria based on our previous experience with other zeolite structures are used to select the most structurally sensible frameworks. Using these criteria, four monoclinic and four orthorhombic frameworks are selected as the most likely candidates. Different intergrowths of these eight possibilities are then investigated using XRD simulations of faulted structures. The agreement between the calculated and experimental patterns is then finally used to fine-tune the faulting probabilities and the relative proportions of the intergrowths present in the structure of SSZ-31.

Development of Possible Framework Structures of SSZ-31. Initially, we use the experimental information presented above to constrain, as much as possible, the tetrahedral frameworks compatible with these data. The models that are consistent with all the requirements are investigated in detail, using the agreement between the simulated and experimental XRD patterns as the criteria to select the most promising candidates.

The unit cell parameters of SSZ-31 derived from X-ray and electron diffraction suggest the presence of structural relationships to other known zeolites. The estimated cell dimension of SSZ-31 along c ($c = 12.33$ Å) is similar to the c cell dimension of ZSM-12[11,19] ($c = 12.25$ Å), and zeolite SSZ-33[8] ($c = 12.35$ Å). Also, the monoclinic angle β of ZSM-12 ($\beta = 108°$) is similar to the angle in SSZ-31 ($\beta = 106°$). ZSM-12 and SSZ-33 are also faulted, as is SSZ-31, and the faulting is such that it does not block the zeolite pores. On the other hand, the cell dimension of SSZ-31 along the pore ($b = 8.38$ Å) is similar to the cell dimension along the channel of several one-dimensional pore high-silica zeolites (ZSM-48, SSZ-24[20] (AFI),

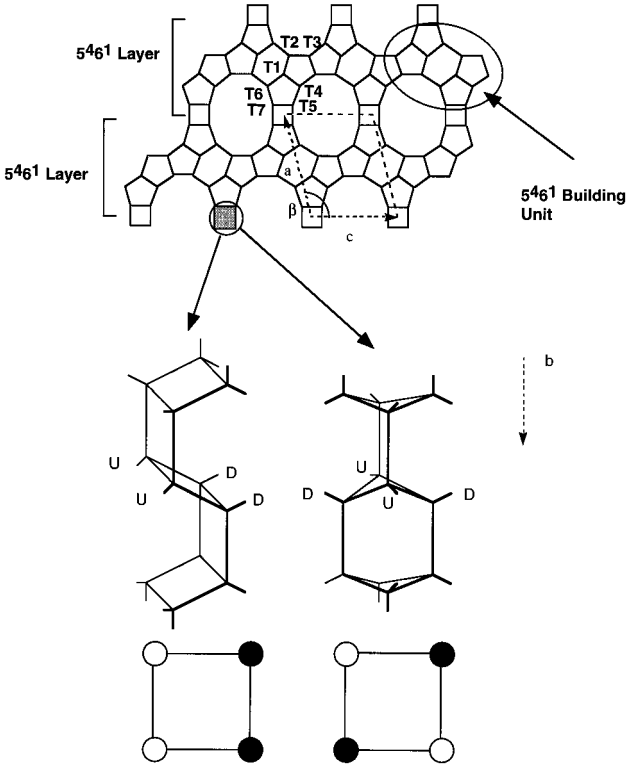

Figure 5. Illustration of the connectivity of the initial trial models of the structure of SSZ-31. Here it is shown the main structural units of the model: the 5^46^1 secondary building unit and the layers that can be formed with this building unit. These 5^46^1 layers are connected via a four-ring. These four-rings can be arranged in the UUDD configuration (double crankshaft chains) or the UDUD configuration (narsarsukite chains). Note also that, as observed in the double crankshaft chain, two consecutive UU or DD T-atoms force the formation of a 4MR in the structure. The numbers indicate the seven crystallographic inequivalent T-atoms of the asymmetric unit.

and UTD-1[21]). These three zeolites are all formed of nets of tetrahedral atoms in up (●) or down (○) combinations. All of these materials are high-silica zeolites, and, therefore, one may expect some structural similarities (*vide infra*). Because of these relations and the results from electron microscopy, the initial trial models are based on the projection of the ZSM-12 zeolite framework along the pore axis but with the T-atoms connected in up or down configurations (see Figure 5). One advantage of this configuration of tetrahedral atoms is that effectively the problem can be cast in two dimensions instead of three.

The number of possible framework models in agreement with these few restrictions is extremely large, and further constrains are needed to reduce the number of possibilities to a manageable level. Inspection of the two-dimensional three-connected net (see Figure 5) shows that there are seven crystallographic inequivalent T-atoms in the asymmetric unit. Because all the T-atoms are arranged in up/down configurations, there must be a mirror plane through the oxygen atoms that link two consecutive layers of up or down T-atoms (a layer parallel to the *ac* plane). It is possible to form 63 ($2^{(7-1)}$-1) frameworks with different up and down configurations using only the restriction of a mirror plane (space group $P2/m$). Therefore, further criteria to select the most likely configurations of the tetrahedral atoms in the framework are still necessary.

The search is restricted to structures in which the channel is formed by a cylindrical six-ring net, since cylindrical nets are found in zeolites ZSM-48 and SSZ-24.[22] Related cylindrical

(19) Meier, W. M.; Olson, D. H. *Atlas of Zeolite Structure Types*, 3rd ed.; Butterworth-Heinemann: Stoneham, MA, 1992.

(20) (a) Bialek, R.; Meier, W. M.; Davis, M. E.; Annen, J. M. *Zeolites* **1991**, *11*, 438. (b) Richardson, J. W.; Smith, J. V.; Han, S. X. *J. Chem. Soc., Faraday Trans.* **1990**, *86*, 2341−2342.

(21) Freyhardt, C. C.; Tsapatsis, M.; Lobo, R. F.; Balkus, K. J., Jr.; Davis, M. E. *Nature* **1996**, *381*, 295−298.

Table 1. Adsorption Capacities for SSZ-31 and Several Other Zeolites

adsorbate	kinetic diameter[a] (Å)	adsorption capacity (mL g^{-1}) SSZ-24 (AFI)	ZSM-12 (MTW)	SSZ-31[b]	ZSM-5 (MFI)	zeolite Y (FAU)
nitrogen	4.4	0.11	0.12	0.12	0.15	0.28
n-hexane	4.4	0.101	0.12		0.17	0.28
cyclohexane	6.0		0.10	0.09	0.04	0.24
2,2-dimethyl-butane	6.2	0.124	0.11	0.10	0.01	0.25

[a] From ref 26. [b] SSZ-31, as zeoliteY, slowly absorbs 1,3,5-triisopropylbenzene at room temperature. After 6 days, a total of 0.063 mL g^{-1} are adsorbed by SSZ-31. This data point is also in agreement with a 12MR pore material.

six-ring nets also form tubular channels in ZSM-12 (MTW), cancrinite (CAN), and several aluminophosphate molecular sieves. The cylindrical six-ring net implies that there must be a strict alternation of UDUD... (○ ● ○ ● ○ ● ...) T-atoms throughout the 12-membered ring (12MR) of the pores of SSZ-31. The presence of two consecutive up or down atoms implies the formation of a 4MR in the pore walls. In addition, since high-silica zeolites show only a relatively small number of four-rings in the structure, the candidate topologies with small number of four-rings are preferred. It is also clear that two types of models can be built; those based on UDUD 4MRs (narsarsukite chains) along the pore axis or those based on UUDD chains (so-called double crankshaft chains) along the pore axis.[22a] Figure 5 shows an illustration of the narsarsukite and double crankshaft chains.

All the proposed structures can be constructed of $5^4 6^1$ layers (parallel to the *bc* plane, see Figure 5) connected to each other via the narsarsukite or the double-crankshaft chains. In what follows, several hypothetical zeolites structures are developed using the constraints implied by the formation of six-ring cylindrical nets and the presence of either narsarsukite or double crankshaft chains. The simulated X-ray powder diffraction patterns of all models are then used to select the most promising candidates for further investigation. However, note at this point that ED and HREM data (*vide supra*) have shown the presence of heavy stacking faults in the overall structure of SSZ-31, and we have not included the faulting in the simulations yet.

Models with Narsarsukite (UDUD) Chains. Two different types of layers connected via narsarsukite chains can be formed. The first layer type, denoted layer α, is depicted in Figure 6a. Consecutive stacking of this type of layer (ααααα...) forms a framework structure with monoclinic symmetry that is from now on called polymorph A (*P*2/*m*, no. 10). Table 2 summarizes unit cell parameters, space group, and other characteristics of polymorph A and all subsequently defined polymorphs. A second layer α′ can be formed by a 2-fold rotation (or mirror plane) operation on layer α (see Figure 6a). As before, consecutive stacking of this layer (α′α′α′α′...) also forms polymorph A. An illustration of the structure of polymorph A is presented in Figure 7.

It is possible to describe polymorph A by the stacking of layers where layer translations, but no rotations, are allowed. With the unit cell axis of polymorph A ($a \cos \beta = {}^1/_3 c$), each layer can be related by translational symmetry to each other by (*i*) a translation of ∼14.4 Å ($a \sin \beta$) perpendicular to the *bc* plane plus (*ii*) a translation ($-{}^1/_3 c = a \cos \beta$) parallel to *c*. This relation will be used to explain the presence of sharp and streaked intensities in the ED patterns.

A new framework topology can be formed by sequential stackings of layers α and α′ in strict alternation, αα′αα′αα′αα′... This type of stacking sequence forms a crystalline structure with orthorhombic symmetry (*Pmna*, no. 53) denoted polymorph B. Both polymorphs, A and B, contain seven inequivalent T-atoms in the asymmetric unit. The atomic positions of the silicon and oxygen atoms optimized using distance least-square optimization routines (DLS-76) are presented in Tables 3 and 4. The two polymorphs are refined to a figure of merit values $r < 10^{-3}$, using Si−O bond distances of 1.60 Å and constant unit cell parameters (as in Table 2) during the optimization.

The second layer-type connected via narsarsukite chains is denoted layer β and is depicted in Figure 6b. As before, there is a corresponding layer β′ that is related to layer β by a 2-fold rotation. The difference between layer β and layer α is observed in the up (●) and down (○) configuration of the 6MRs. In the α layer, the configuration of the 6MR is (● ● ○ ● ● ○) and includes two 4MRs perpendicular to the *ac* plane. In layer β, the configuration of the 6MR is (● ○ ● ○ ● ○) and does not contain 4MRs. Similar to what has been found for the case with layers α and α′, it is possible to form two different crystalline structures with the layers β and β′. If the layers are stacked in a ββββ... or β′β′β′β′... configuration, a monoclinic polymorph C is formed; but if the layers are stacked in a ββ′ββ′... configuration, an orthorhombic polymorph D is formed. The unit cell parameters and space groups of the monoclinic polymorph C (*C*2/*m*) and the orthorhombic polymorph D (*Pbcm*) are summarized in Table 2 For all cases, the standard setting of the space groups are used. Therefore, Figure 6 needs to be consulted to determine the direction of the unit cell parameters *a*, *b*, and *c*.

The cell dimension along *a* has to be doubled for the monoclinic polymorph C, because the narsarsukite chains between two consecutive β layers are related to each other by a vector that includes a translation of $\pm{}^1/_2 b$. The atomic positions of the silicon and oxygen atoms of polymorphs C and D, optimized using DLS-76, have been deposited as Supporting Information.

Figure 8a compares the simulated X-ray powder diffraction patterns of these four polymorphs to the experimental synchrotron XRD pattern of SSZ-31. Several similarities can be observed between the two monoclinic polymorphs A and C and the experimental pattern. The position of the first few reflections as well as the relative intensity of many of the intense reflections are very similar in both polymorphs. Additionally, many of these reflections are also present in the experimental pattern. There are, of course, many reflections in the calculated XRD patterns that are not observed in the experimental pattern. These differences are due to the disorder and the heavy stacking faults in the structure of SSZ-31 and will be explored in following sections. Because of their relative similarity to the experimental XRD, the two monoclinic polymorphs A and C will be the used as the basis for the simulation of the disordered structures (*vide infra*). In contrast to the two monoclinic polymorphs, comparison of the positions of the first few reflections of the two orthorhombic polymorphs clearly shows marked differences to the experimental XRD pattern of SSZ-31.

(22) Higgins, J. B. In *Silica: Physical Behavior, Geochemistry and Materials Applications*; Heaney, P. J., Prewitt, C. T., Gibbs, G. V., Eds.; Mineralogical Society of America: Washington D.C., 1994.

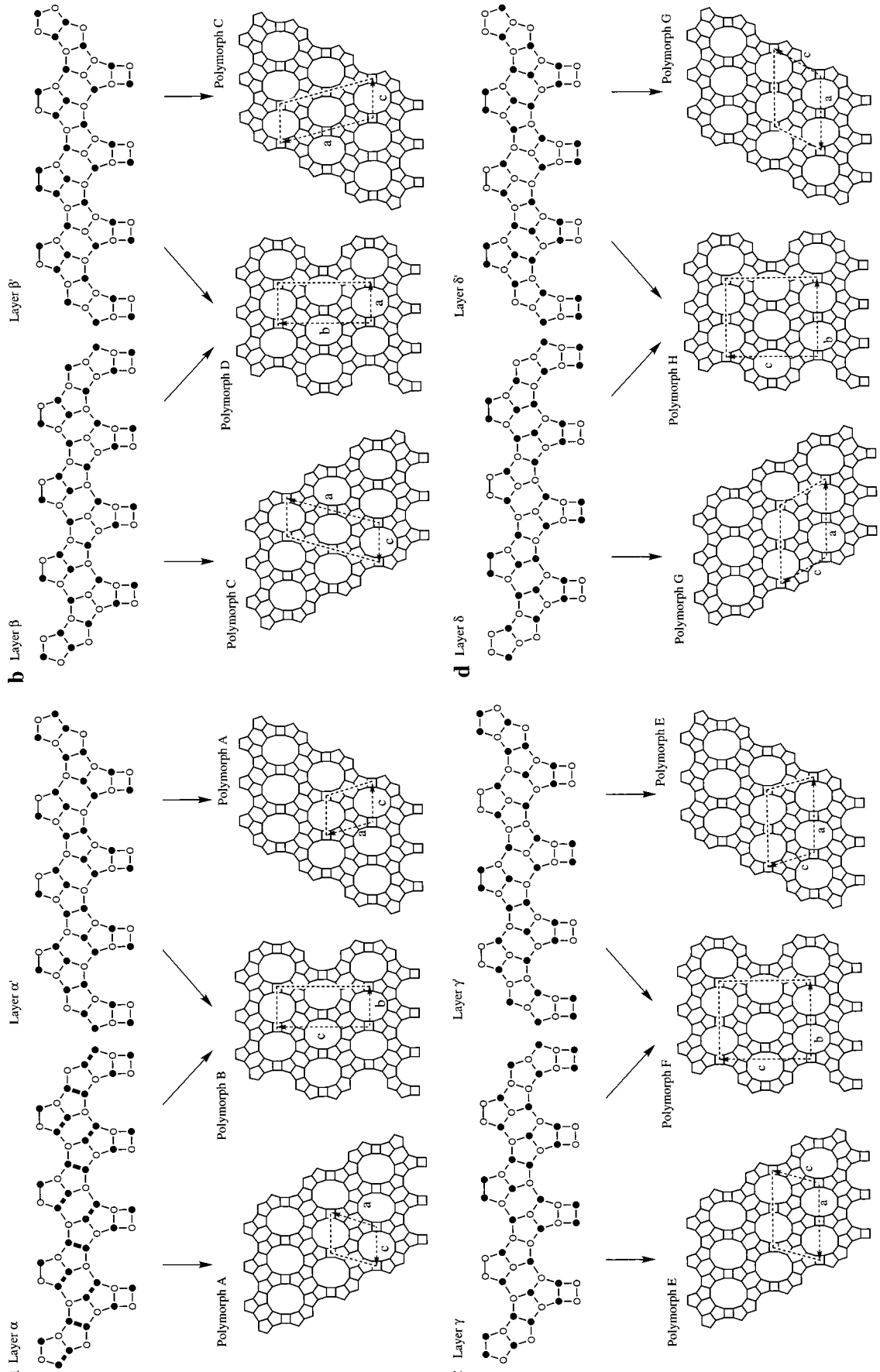

Figure 6. Illustration of "pure" crystalline polymorphs consistent with the unit cell dimensions of SSZ-31 and with pores formed of cylindrical six-ring nets. (a) Up (●) and down (○) configuration of tetrahedral atoms of layers α and α′ and the stacking of the layers to form polymorphs A and B. The thick lines are drawn to illustrate the formation of 4MR in the structure. (b) Up and down configuration of T-atoms of layers *β* and *β*′ and polymorphs C and D. (c) Up and down configuration of T-atoms of layers *γ* and *γ*′ and polymorphs E and F. (d) Up and down configuration of T-atoms of layers *δ* and *δ*′ and polymorphs G and H. The intent of the drawing of the unit cell axes is to show the relative sizes and directions of the unit cell. The origin of the crystallographic unit cell does not correspond in all cases to the center of the 4MR of the structure (as drawn) and depends on the particular space group of each framework topology.

Table 2. Summary of Characteristics of Possible Framework Structures of SSZ-31[a]

polymorph	crystal system	space group (no.)	cell dimensions	unit cell content	unit cell volume (Å^3)
A	monoclinic	*P*2/*m* (10)	$a = 14.92$ Å $b = 8.38$ Å $c = 12.35$ Å $\beta = 106°$	$Si_{28}O_{56}$	1493
B	orthorhombic	*Pmna* (53)	$a = 8.38$ Å $b = 12.35$ Å $c = 28.78$ Å	$Si_{56}O_{122}$	2986
C	monoclinic	*C*2/*m* (12)	$a = 29.93$ Å $b = 8.38$ Å $c = 12.35$ Å $\beta = 106°$	$Si_{56}O_{122}$	2986
D	orthorhombic	*Pbcm* (57)	$a = 12.35$ Å $b = 28.78$ Å $c = 8.38$ Å	$Si_{56}O_{122}$	2986
E	monoclinic	*C*2/*m* (12)	$a = 14.92$ Å $b = 8.38$ Å $c = 24.70$ Å $\beta = 106°$	$Si_{56}O_{112}$	2986
F	orthorhombic	*Cmca* (64)	$a = 8.38$ Å $b = 24.75$ Å $c = 28.78$ Å	$Si_{112}O_{224}$	5972
G	monoclinic	*C*2/*m* (12)	$a = 24.75$ Å $b = 8.38$ Å $c = 16.58$ Å $\beta = 119.8°$	$Si_{56}O_{122}$	2986
H	orthorhombic	*Cmca* (64)	$a = 8.38$ Å $b = 24.70$ Å $c = 28.78$ Å	$Si_{112}O_{224}$	5972

[a] All the materials have a density of $\rho = 1.87$ g cm^{-3} and a framework density of FD = 18.7 T nm^{-3} and contain seven independent T-atoms in the asymmetric unit.

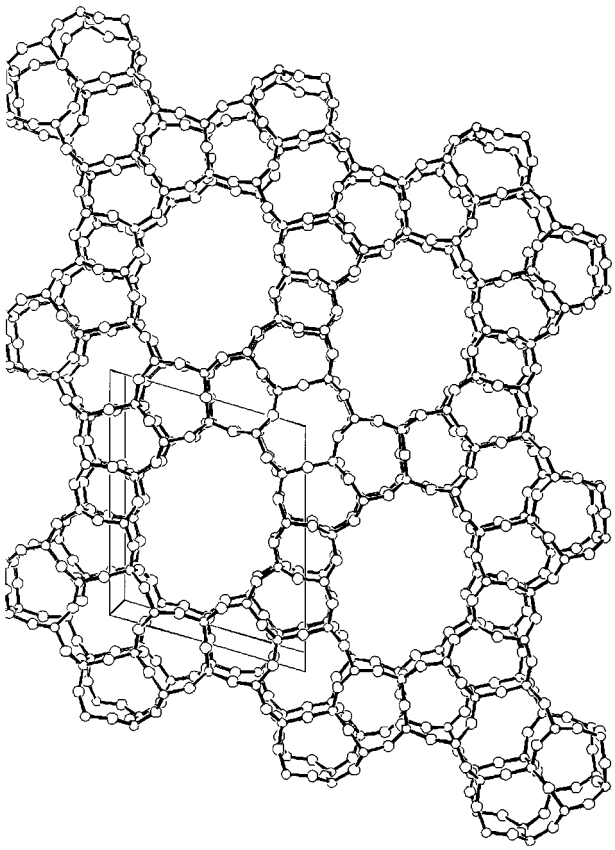

Figure 7. Framework structure of polymorph A.

Models with Double Crankshaft (UUDD) Chains. If the connection of the 5^46^1 layers is carried out using the double crankshaft chains, two other layer types (γ and δ) are formed. Stacked together, these layers also form crystalline structures with cylindrical six-ring net pores. The δ and γ layers as well as the corresponding δ' and γ' layers are illustrated in Figure 6c,d. In a way completely analogous to that described in the previous section for layers α and β, consecutive stackings of $\gamma\gamma\gamma\gamma$... and $\delta\delta\delta\delta$... layers form two monoclinic polymorphs (denoted polymorph E and polymorph G) and stacking of $\delta\delta'\delta\delta'$... and $\gamma\gamma'\gamma\gamma'$... layers form two orthorhombic polymorphs (denoted F and H). The unit cell dimensions and the space groups of these four polymorphs are summarized in Table 2. The DLS-76 optimized atomic positions of the asymmetric unit of the four polymorphs have been deposited as Supporting Information. Figure 8b compares the simulated X-ray powder diffraction patterns of these four polymorphs with the experimental synchrotron XRD pattern of SSZ-31. There are clear similarities between the XRD patterns of the two monoclinic polymorphs (E and G) and the experimental pattern of SSZ-31; it is also clear that there are significant differences between the XRD patterns of the orthorhombic polymorphs and the experimental pattern.

In addition to the four layers α, β, γ, and δ described here, there are four other layers that also form cylindrical six-ring net pores. These additional layers can be derived from the previous four by changing the T-atom **1** (as indicated in Figure 5) from an up to a down configuration or vice versa. However, this change forms two or three additional 4MRs per 5^46^1 unit. We consider this possibility unlikely due to the strain associated with the presence of several consecutive 4MR in the structure. These layers have not been investigated further.

In summary, it has been shown that using simple criteria for selecting structurally sound framework topologies for SSZ-31, a very large number of possible frameworks can be reduced to eight polymorphs. Simulation of the XRD patterns of these eight polymorphs shows that the four orthorhombic models are not viable alternatives for the structure of SSZ-31. This result is also in agreement with the ED and HREM data that show, despite the presence of heavy stacking faults, a predominance

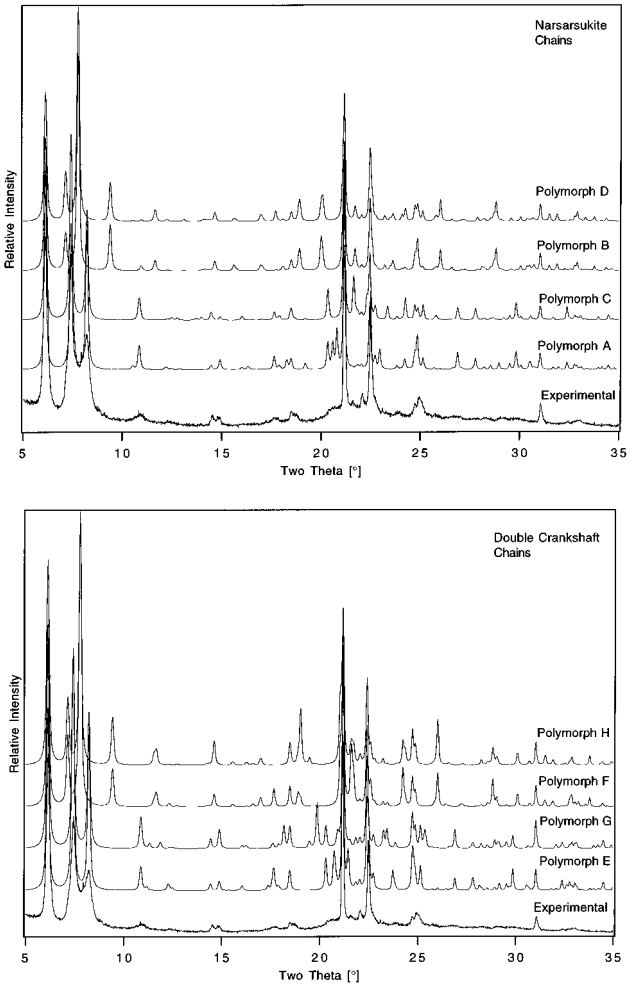

Figure 8. (a) Simulated XRD patterns of polymorphs A, C, B, and D and experimental pattern of SSZ-31. (b) Simulated XRD patterns of polymorphs E, G, F, and H and experimental pattern of SSZ-31.

of monoclinic polymorphs in the structure of SSZ-31. All the models provide a crystallographic density of $\rho = 1.87$ g cm^{-3} and a framework density of FD = 18.7 T nm^{-3}. The pore apertures are elliptical with major and minor axis of approximately 8.6 Å × 5.7 Å. This aperture is intermediate between the pore size of ZSM-12 (MTW, 6.2 Å × 5.5 Å) and SSZ-24 (AFI, 7.3 Å)[19] and is consistent with the size and shape of the structure-directing agents and the adsorption results (Table 1).

At this point, it is not possible to discriminate between the four different monoclinic polymorphs (A, C, E, and G), or combinations thereof, as far as which is a better representation of the structure of SSZ-31, because of the effect of faulting on the XRD patterns. In the next section, the effect of faulting on the XRD pattern of polymorphs A, C, F, and G is investigated in detail. The simulated XRD patterns of the faulted structures are then used to select which of the four alternatives is (are) the most likely topology(ies).

Simulation of X-ray Powder Diffraction Patterns: The Effect of Faulting and Disorder. The effect of faulting on the XRD pattern of each polymorph is simulated using the program DIFFaX. In this program, planar intergrowths are described in terms of layer stackings and stacking vectors. The plane of the layer must be described in terms of the axis *a* and *b*, and the stacking direction *c* is perpendicular to the *ab* plane, i.e., $c/|c| = (a \times b)/|a \times b|$. We have followed Treacy et al. in the description of the disorder (see ref 9a for more details). The cell dimensions used to describe the layers are $a = 12.35$ Å, $b = 8.38$ Å, $c = 14.4$ Å, and $\gamma = 90°$ for layers α, α′, β, and β′ and $a = 8.38$ Å, $b = 24.74$ Å, $c = 28.8$Å and $\gamma = 90°$ for layers δ, δ′, γ, and γ′. The origin of the layer is the center of the 4MRs, and the coordinates of the atomic positions have been corrected to reflect this change. The stacking vector is such that the 4MR at the top of one layer connect to the corresponding 4MR at the bottom of the next layer forming the narsarsukite chains or the double crankshaft chains.

For the case of intergrowths of layers α and α′, the polymorph A is built by recurrently stacking layers α as shown in Figure

Table 3. Atomic Positional Parameters of Polymorph A

atom	multiplicity and Wyckoff letter	*x*	*y*	*z*
Si1	4o	0.8899	0.1841	0.1404
Si2	4o	0.7811	0.8162	0.8831
Si3	4o	0.5939	0.3147	0.9047
Si4	4o	0.5974	0.8172	0.1363
Si5	4o	0.7712	0.3165	0.2920
Si6	4o	0.9027	0.8125	0.5119
Si7	4o	0.0866	0.6860	0.2465
O1	2m	0.8883	0.0000	0.1698
O2	2m	0.7831	0.0000	0.8532
O3	2n	0.5866	0.5000	0.8775
O4	2m	0.5951	0.0000	0.1023
O5	2n	0.7440	0.5000	0.2843
O6	2m	0.8962	0.0000	0.4941
O7	2n	0.0737	0.5000	0.2606
Oa	4o	0.4988	0.2302	0.8413
Ob	4o	0.9946	0.2422	0.1638
Oc	4o	0.8209	0.2712	0.4193
Od	4o	0.8399	0.2829	0.2168
Oe	4o	0.8368	0.2112	0.0113
Of	4o	0.6137	0.2888	0.0368
Og	4o	0.8282	0.7159	0.8044
Oh	4o	0.0000	0.7509	0.5000
Oi	4o	0.6764	0.7602	0.8634
Oj	4o	0.8937	0.7703	0.6340
Ok	4o	0.6797	0.7878	0.2474

[a] Space group *P*2/*m* (no. 10) $a = 14.92$ Å, $b = 8.38$, $c = 12.35$ Å, $\beta = 106°$.

Table 4. Atomic Positional Parameters of Polymorph B

atom	multiplicity and Wyckoff letter	*x*	*y*	*z*
Si1	8i	0.1822	0.2065	0.0378
Si2	8i	0.3144	0.0383	0.1077
Si3	8i	0.3185	0.8140	0.0591
Si4	8i	0.3143	0.4400	0.0465
Si5	8i	0.1845	0.3830	0.8890
Si6	8i	0.1886	0.9637	0.2005
Si7	8i	0.3110	0.7233	0.2013
O1	4h	0.0000	0.1952	0.0236
O2	4h	0.5000	0.0615	0.1035
O3	4h	0.5000	0.7848	0.0685
O4	4h	0.5000	0.4156	0.0448
O5	4h	0.0000	0.4102	0.8849
O6	4h	0.0000	0.9732	0.1985
O7	4h	0.5000	0.7295	0.2016
Oa	8i	0.2082	0.7188	0.0778
Ob	8i	0.2182	0.1305	0.0812
Oc	8i	0.2192	0.3290	0.0512
Od	8i	0.2397	0.8410	0.1925
Oe	4g	0.2500	0.0030	0.2500
Of	4g	0.2500	0.6790	0.2500
Og	8i	0.2540	0.3562	0.8390
Oh	4f	0.2619	0.5000	0.0000
Oi	8i	0.2647	0.0375	0.1610
Oj	8i	0.2748	0.9237	0.0852
Ok	8i	0.2758	0.5153	0.0899
Ol	8i	0.2912	0.1712	0.9952

[a] Space group *Pmna* (no. 53) $a = 8.38$ Å, $b = 12.35$ Å, $c = 28.78$ Å.

6a. The stacking vectors $\mathbf{R}_{ij}$ connecting layer structures i and j are for this case

$$\mathbf{R}_{\alpha\alpha} = \mathbf{R}_{\alpha\alpha'} = -{}^1/_3 a + c$$

$$\mathbf{R}_{\alpha'\alpha} = \mathbf{R}_{\alpha'\alpha'} = {}^1/_3 a + c$$

Since the results from the HREM do not show any long range order, it is assumed that the layers are randomly distributed, and a simple stacking probability p is used to describe the random sequences of layers α and α′. The stacking probability $p = p_{\alpha\alpha'} = p_{\alpha'\alpha}$ is the probability that a layer α is connected to a layer α′ and vice versa, forming a sheet of polymorph B. If $p = 0$, the stacking of layers is equivalent to a crystal formed of long sections of polymorph A. If $p = 1$, it is equivalent to a crystal formed of long sections of polymorph B. Finally, if $p = 0.5$, it is equivalent to a fully random intergrowth of layers α and α′ (A diagram illustrating a stacking sequence with $p = 0.25$ has been deposited as Supporting Information).

The results from the simulations of XRD patterns for intergrowths of layers α and α′ with stacking probabilities from 0 to 50% are shown in Figure 9.[23] An estimate of the stacking probability of the experimental XRD pattern of SSZ-31 can be obtained from these simulations by inspection of the relative intensity of the first three peaks of the pattern. The simulated pattern with a stacking probability of 20−25% gives, approximately, the observed relative intensity of these first three reflections. This stacking probability is in qualitative agreement with the observations from HREM of SSZ-31.

Similar calculations have been carried out for layers β and β', γ and γ', and δ and δ'. The stacking vectors for these layer intergrowths are respectively

$$\mathbf{R}_{\beta\beta} = \mathbf{R}_{\beta\beta'} = -{}^1/_3 a + {}^1/_2 b + c$$

$$\mathbf{R}_{\beta'\beta} = \mathbf{R}_{\beta'\beta'} = {}^1/_3 a + {}^1/_2 b + c$$

$$\mathbf{R}_{\gamma\gamma} = \mathbf{R}_{\gamma\gamma'} = -{}^1/_6 b + {}^1/_2 c$$

$$\mathbf{R}_{\gamma'\gamma} = \mathbf{R}_{\gamma'\gamma'} = {}^1/_6 b + {}^1/_2 c$$

$$\mathbf{R}_{\delta\delta} = \mathbf{R}_{\delta\delta'} = {}^1/_2 a - {}^1/_6 b + {}^1/_2 c$$

$$\mathbf{R}_{\delta'\delta} = \mathbf{R}_{\delta'\delta'} = {}^1/_2 a + {}^1/_6 b + {}^1/_2 c$$

The stacking vectors for layers γ and γ' and δ and δ' differ from the stacking vectors from layers α and α′ and β and β' because the orthorhombic unit cells of polymorphs F and H were used to describe the layers. Examples of the input files of DIFFaX for the four polymorphs have been deposited as Supporting Information.

The results for the three cases follow the same trends observed for intergrowths of layers α and α′. The relative intensities of the first three reflections are very similar for all the intergrowths, and a comparison of these intensities with the experimental XRD pattern shows that for each case, a good agreements between experimental and calculated XRD patterns are obtained for stacking probabilities of $p \sim 20-25\%$. Using these simulations, it is now possible to identify if any of the faulted polymorphs show a XRD pattern in close agreement with the experimental pattern of SSZ-31. A comparison between experimental and

(23) Layer atomic positions: The atomic positions of the silicon and oxygen atoms of each layer were directly obtained from the DLS-76 optimized positions of the orthorhombic polymorphs B, D, F, and H. This was done due to the simplicity of orthogonal coordinates of this system. The orthorhombic polymorphs contain in one unit cell the two relevant layers for the simulation (say α and α′, for example).

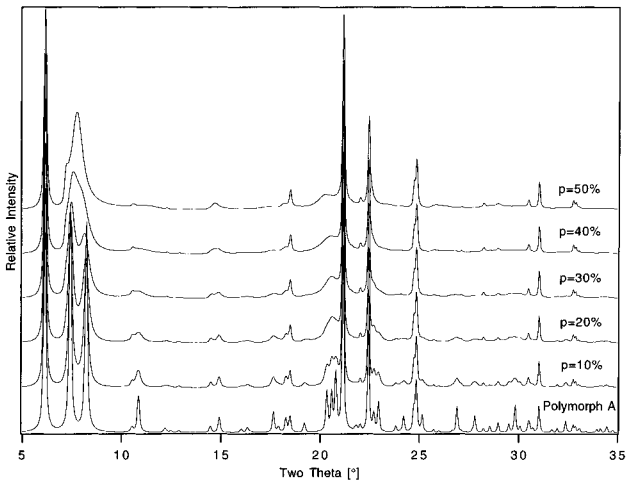

Figure 9. X-ray powder diffraction patterns of intergrowths of layers α and α′ as a function of the fault probability p.

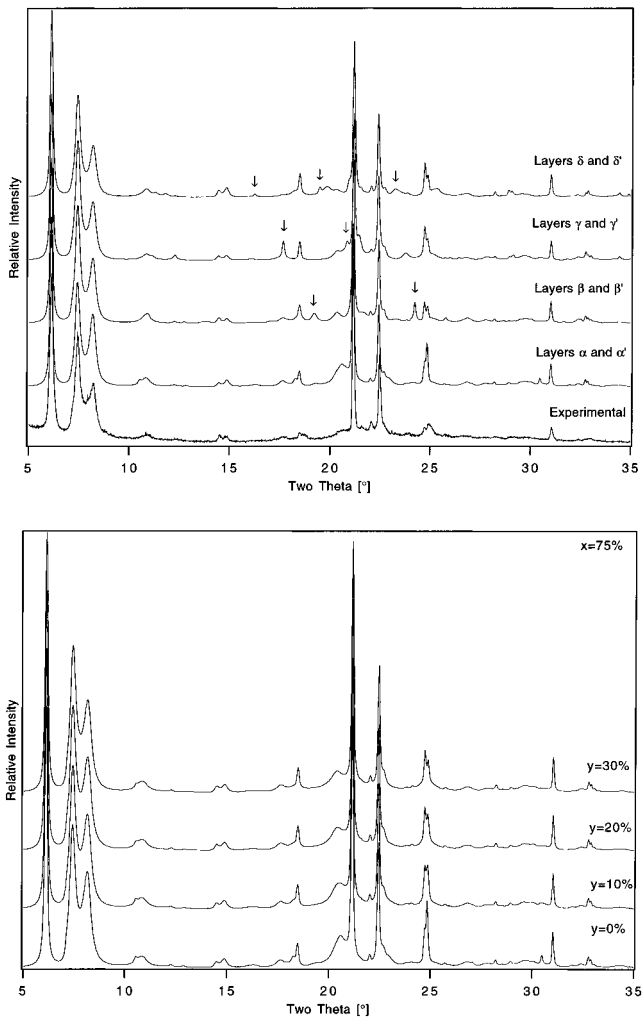

Figure 10. (a) Comparison between experimental and calculated XRD patterns for intergrowths of different layer types. In all cases the stacking probability is $p = p_{ii'} = p_{i'i} = 20\%$, where $i = \alpha, \beta, \gamma, \delta$ and $i' = \alpha', \beta', \gamma'$, and δ'. From the bottom: experimental XRD pattern of SSZ-31, and intergrowth of layers α and α′, β and β', γ and γ', and δ and δ'. (b) XRD patterns of intergrowths of layers α, α′, β and β' as a function of the parameter y, the fraction of layers β and β'. The parameter x is kept constant at $x = 0.75$ for all the calculations.

calculated patterns for materials with a stacking probability of 20% is presented in Figure 10a. Although at low angles all the patterns are essentially the same, differences become evident at angles higher than 17° 2Θ. In particular, intergrowths of layers γ and γ' show a strong reflection at ∼18° 2Θ and two weaker peaks at 20° and 21° 2Θ which are absent in the experimental XRD pattern. Intergrowths of layers δ and δ' show broad peaks at 19° and 20° 2Θ, and intergrowths of layers β and β' show differences to the experimental pattern at 24° 2Θ and a broad peak at 19° 2Θ (these differences are marked in Figure 10a with an arrow). The most similar calculated XRD pattern corresponds to intergrowths of layers α and α′, and, therefore, it is concluded that of the four faulted polymorphs investigated, the XRD pattern of faulted polymorph A shows the best qualitative agreements to the experimental pattern of SSZ-31.

The faulted polymorph A model of the structure of SSZ-31, consisting of stackings of layers α and α′ with a stacking probability $p_{\alpha\alpha'} = p_{\alpha'\alpha} = 20-25\%$, is in agreement with most of the available experimental information. In addition to qualitative agreement of the adsorption capacity, the unit cell dimensions, and the simulated and experimental XRD patterns, this model also predicts the presence of sharp and streaked intensities in the ED pattern, with sharp spots for every third column (*hk*3*n*). This is because the relative displacement for successive layers is one-third of the intralayer spacing, i.e., a translation of $\pm^1/_3 c = |a| \cos\beta$ as discussed previously.[24] There are, however, disagreements with some of the experimental evidence. For example, the center of the broad peak at ∼20.5° 2Θ is, more precisely, at 20.51° 2Θ in the experimental patterns (see Figure 1a) but is observed at 20.59° 2Θ in the calculated XRD with $p_{\alpha\alpha'} = 20-25\%$. It is also clear that there is more "structure" in the calculated XRD pattern of intergrowths of layers α and α′ than in the experimental patter. These differences suggest the presence of additional disorder in the structure of SSZ-31 associated with layers containing different up or down atom configurations, i.e., containing in addition to layers α and α′, a small fraction of, most likely, layers β and β'. It is possible to go from stackings of layers α to stackings of layers β maintaining the cylindrical six-ring nets that form the pores and the narsarsukite chain connectivity between the layers (see Supporting Information). Further refinements are then necessary in the structure model of SSZ-31. It is also *not* possible to form intergrowths of layers α, with layers δ or γ, without forming a 4MR in the pore walls.

Simulation of X-ray Powder Diffraction Patterns of Intergrowths Containing Layers α, α′, *β*, and *β*′. In order to carry out simulations of intergrowths of layers α, α′, β, and β', it is necessary to define in addition to the atomic positions of the silicon and oxygen atoms for each of the four layers, a matrix of stacking vectors, $\mathbf{R}_{ij}$, and a matrix of stacking probabilities, p_{ij}.[25] The stacking vectors, $\mathbf{R}_{ij}$, connecting layer structures *i* and *j* are given by

$$\mathbf{R}_{\alpha j} = -^1/_3 a + c$$

$$\mathbf{R}_{\alpha' j} = {}^1/_3 a + c$$

$$\mathbf{R}_{\beta j} = -^1/_3 a + {}^1/_2 b + c$$

$$\mathbf{R}_{\beta' j} = {}^1/_3 a + {}^1/_2 b + c$$

with $j = \alpha, \alpha', \beta, \beta'$ and with the cell dimensions used before to describe the layers ($a = 12.35$ Å, $b = 8.38$ Å, $c = 14.4$ Å, and $\gamma = 90°$). Note that one of the assumptions implicit in this model is that each layer in the structure is *only* of type α or of type β, i.e., that there are no transitions from α to β within one layer. We have no experimental evidence to validate or disprove this assumption. This type of disorder cannot be simulated in the current version of DIFFaX.

If it is assumed that the stacking sequence is completely random, then the constrains on the stacking probability "phase space" are simply

$$\sum_{j=\alpha,\alpha',\beta,\beta'} p_{ij} = 1 \quad \text{for } i = \alpha, \alpha', \beta, \beta'$$

and, because of the symmetry of layers α, α′ and layers β, β', $p_{\alpha\alpha} = p_{\alpha'\alpha'}$, $p_{\alpha\alpha'} = p_{\alpha'\alpha}$, $p_{\beta\beta} = p_{\beta'\beta'}$, $p_{\beta\beta'} = p_{\beta'\beta}$, $p_{\alpha\beta} = p_{\alpha'\beta'}$, $p_{\alpha\beta'} = p_{\alpha'\beta}$, $p_{\beta\alpha} = p_{\beta'\alpha'}$, $p_{\beta\alpha'} = p_{\beta'\alpha}$. These 12 equations reduce the number of variable parameters in the stacking probability matrix from 16 to four.

The fraction of the total of number of layers of the crystallite of type *j* is given by

$$g_j = \Big(\sum_{i=\alpha,\alpha',\beta,\beta'} p_{ij}\Big)/4 \quad \text{for } j = \alpha, \alpha', \beta, \beta' \;\therefore \sum_{j=\alpha,\alpha',\beta,\beta'} g_j = 1$$

Again, because of the symmetry of layers α, α′ and β, β' we have $g_\alpha = g_{\alpha'}$ and $g_\beta = g_{\beta'}$.

As an example of the effect that intergrowths of two types of layers may have on the XRD patterns a series of intergrowths of layers α and β, i.e., intergrowths of polymorphs A and C have been simulated. It is assumed that the stacking of layers α and β is completely random. From the simulations (see Supporting Information) it is concluded that this type of stacking makes little change in the relative intensity of the first few reflections—*1 0 0*, *0 0 1*, and *1 0* $\bar{1}$. This can be understood in terms of the differences between layers α and β. These differences involve mostly translations of Si and O atoms along the pore. This kind of change in electron density distribution in the asymmetric unit does not affect the structure factors of indexes *h*0*l*. Note that in terms of the projection of the electron density distribution along the crystal pores, polymorphs A and C are almost indistinguishable.

Now, to ascertain the effect on the XRD pattern of including a fraction of layers β and β' in an intergrowth of mainly layers α and α′—such that the relative intensity of the first three peaks of the simulated XRD do not change—two new parameters are defined

$$x = p_{\alpha\alpha} + p_{\alpha\beta} = p_{\alpha'\alpha'} + p_{\alpha'\beta'} = p_{\beta\alpha} + p_{\beta\beta} = p_{\beta'\alpha'} + p_{\beta'\beta'}$$

$$y = g_\beta + g_{\beta'} = 2g_\beta$$

where *x* is the fraction of "monoclinic" polymorphs in the crystallites (i.e., the probability of going from layer α or β, to layer α or β) and *y* is the fraction of layers β and β'. Using these two additional equations, the matrix of stacking probabilities is defined in terms of only two parameters

(24) We have also carried out simulations of ED patterns of the four faulted polymorphs along [0 1 0] and [1 0 0] using DIFFaX. The ED patterns along [0 1 0], the pore direction, show sharp spots for every third column, *hk*3*n*, and streaks for the other columns in the four cases. The ED patterns along this direction are qualitatively very similar for the four intergrowths. ED patterns along [1 0 0] show sharp spots every other column *2nkl*, as in Figure 4b, for the four intergrowths. The four patterns along [1 0 0] are also qualitatively very similar. Thus, the ED data cannot be used to select amongst the four faulted models.

(25) See the manual for DIFFaX by M. M. J. Treacy and ref 6a for more details about the stacking vectors and the matrix of stacking probabilities.

(26) Breck, D. W. *Zeolite Molecular Sieves: Structure, Chemistry and Use*, 1st ed.; Wiley: New York; p 770.

$$p_{ij} = \begin{bmatrix} x(1-y) & (1-x)(1-y) & xy & (1-x)y \\ (1-x)(1-y) & x(1-y) & (1-x)y & xy \\ x(1-y) & (1-x)(1-y) & xy & (1-x)y \\ (1-x)(1-y) & x(1-y) & (1-x)y & \text{xy} \end{bmatrix}$$

The relative intensity of the first three peaks, to a first approximation, depends on the value of x only.

Figure 10b shows the calculated XRD patterns for intergrowths with a constant parameter $x = 0.75$ and as a function of the fraction of layer β and β' (ranging from $y = 0-0.3$). Clearly, there is an improvement in the agreement between the calculated and experimental XRD patterns for $y = 0.10-0.15$. The doublet at ~25° 2Θ is now reproduced in the calculated XRD, the sharp peak at 31° 2Θ decreases in intensity, and the center of the broad peak at 20.59° 2Θ now shifts to 20.50° 2Θ as observed experimentally. By inspection, the best agreement between the experimental and calculated XRD patterns is obtained for $x \sim 0.75-0.80$ and $y \sim 0.10$. Therefore, SSZ-31 contains approximately 60.7% of polymorph A ($(1-y)\cdot p_{\alpha\alpha}$), 20.2% of polymorph B ($(1-y)\cdot p_{\alpha\alpha'}$), 0.75% of polymorph C ($y\cdot p_{\beta\beta}$), and 0.25% of polymorph D ($y\cdot p_{\beta\beta'}$). The remainder of the material is composed of isolated layers of β or β' that cannot be described as being part of any of the polymorphs defined previously.

Finally, the effect of the crystal size on the XRD patterns was investigated using the finite layer widths option of DIFFaX, assuming that the crystallite morphology is approximately spherical (see Supporting Information). An improvement of the matching between the experimental and calculated XRD patterns is, by inspection, obtained for an average crystal size of 800−1000 Å. This crystal size is approximately the size estimated from the bright-field images from electron microscopy (Figure 2) for the elongated needles.

It is, of course, still possible to increase the complexity of the model. For example, it can be envisioned that there is a clustering of faults of the layers α and α′, on the one hand, or β and β', on the other hand, which cannot be differentiated by electron microscopy. It is possible that the stacking probability $p_{\alpha\beta'} = p_{\alpha'\beta} \sim 0\%$, and that $p_{\alpha\beta} = p_{\alpha\beta} \sim 10\%$, etc. However, given the quality of the samples, the available experimental data, the number of assumptions that have already been taken, and the good agreement that has been obtained with the current model, the addition of further degrees of freedom to the system is not justifiable.

The basic units of the structure of zeolite SSZ-31 shows several striking similarities to other known high-silica zeolites. First, the projection of the topology of SSZ-31 (polymorph A) along the pore is the same as projection of zeolites ZSM-12 and beta (polymorph B, see Figure 11a). The unit cell dimensions along the pore are 5 Å (ZSM-12), 8.4 Å (SSZ-31), and 12.7 Å (beta) and, therefore, the main difference between these zeolites is the connectivity of the T-atoms down the pore direction. Zeolites SSZ-24 and SSZ-31 also show several similarities (Figure 11b). The two zeolites are formed of T-atoms in up and down configurations. The connectivities of the T-atoms of the pores are also topologically the same: they are formed by a cylindrical net of six-rings, and SSZ-24 and SSZ-31 have among their structural units the narsarsukite chain running down the pore direction. The pore opening of SSZ-24 is very symmetrical with a pore diameter of 7.3 Å, but the pores of SSZ-31 are elongated with an open diameter of 8.6 Å × 5.7 Å.

Finally, SSZ-31 bridges a gap between the structure of zeolite ZSM-48 and UTD-1. The three zeolites are formed of T-atoms

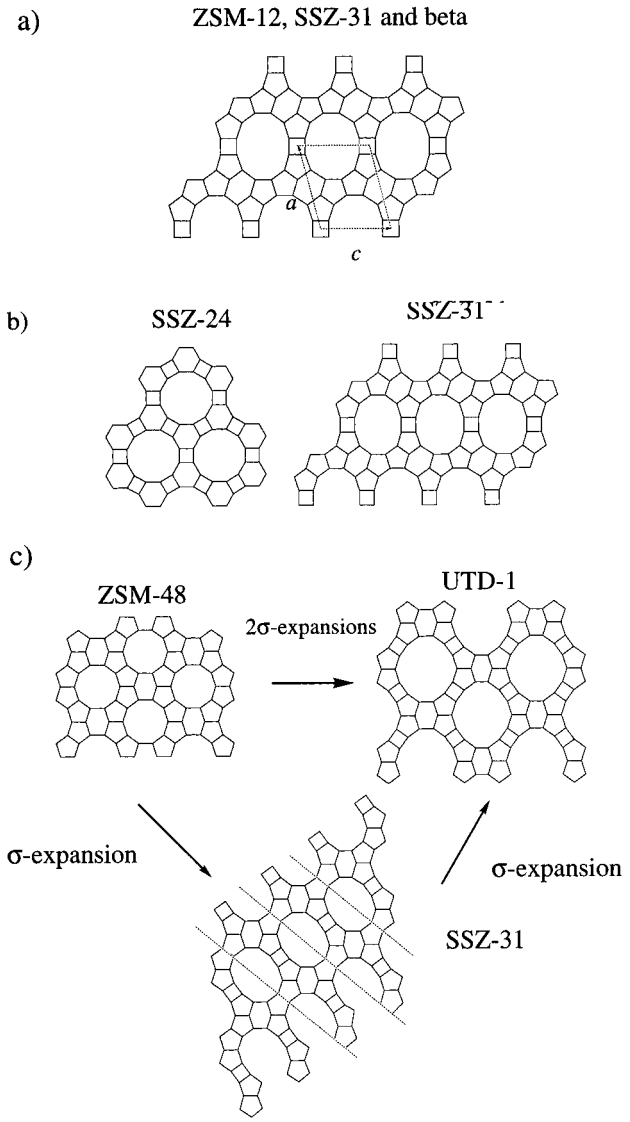

Figure 11. Comparison of framework structures related to SSZ-31: (a) Projection of the framework of zeolites ZSM-12, SSZ-31 and beta along the pores; (b) projection of the framework of SSZ-24 and SSZ-31 along the pores; and (c) comparison of the framework projections of zeolites ZSM-48, SSZ-31, and UTD-1.

in up or down conformations. It has been indicated that the structure of the zeolite UTD-1 can be envisioned as the result of two σ-expansions of the two-dimensional three-connected topology of ZSM-48 along the {1 1 0} planes. In Figure 11c, we show how the structure of SSZ-31 can be envisioned as the σ-expansion of the projection of ZSM-48 along (1 1 0) and that an additional σ-expansion of SSZ-31 now forms the projection of the zeolite UTD-1. In addition, the pores of these three zeolites are formed of the cylindrical six-rings nets mentioned previously, and the main structural unit is the so-called $5^4 6^1$ tertiary building unit.

Summary

Using adsorption capacity measurements, electron diffraction, high-resolution electron microscopy, and X-ray diffraction we have shown that SSZ-31 is a high-silica zeolite with a large one-dimensional pore system. The pore apertures are elliptical with major and minor axes of approximately 8.6 × 5.7 Å. The two-dimensional three-connected projection of the structure down the pores is the same as the projection of zeolites ZSM-12 and beta. The material is heavily faulted. The structure of

SSZ-31 can be described as an intergrowth of four different but structurally related polymorphs, called here polymorphs A, B, C, and D. The pores of the zeolite are formed by a cylindrical six-ring net of T-atoms connected by a narsarsukite chain that runs down the pore direction. SSZ-31 is the most disordered zeolite structure reported to this date. The structure is related to the structures of ZSM-12 and beta but, in addition, is closely related to the structure of the zeolite SSZ-24 (AFI) and the zeolites ZSM-48 and UTD-1. The structure of the zeolite NCL-1 is possibly similar to the structure of SSZ-31. Energy minimization calculations show that the size and shape of the structure-directing agents fits very closely the geometry of the one-dimensional channels. Due to the very large pore diameter of SSZ-31 and the very small crystal size, this material is expected to be a good solid-acid catalyst with unique selectivity.

Acknowledgment. We thank P. Wagner (CIT) who helped to obtain several of the in-house XRD patterns of SSZ-31 and Y. Nakagawa and L. T. Yuen (Chevron) for the synthesis of several of the samples of SSZ-31 used in this work. R. C. Medrud (Chevron) helped to obtain the synchrotron XRD pattern of SSZ-31. We acknowledge D. E. Cox for assistance in collecting the synchrotron data. The XRD data were collected at X7A beam line, National Synchrotron Light Source, Brookhaven National Laboratory, which is supported by the Department of Energy, Division of Materials Sciences and Division of Chemical Sciences. R.F.L. is grateful to the University of Delaware Research Foundation and to Chevron Research and Technology for financial support. M.T. is grateful to the David and Lucile Packard Foundation for a Fellowship in Science and Engineering and to the National Center for Electron Mcroscopy for a NCEM/DOE Fellowship. We thank the W. M. Keck Polymer Morphology Laboratory for use of EM facilities.

Supporting Information Available: Tables of atomic positional parameters of polymorphs C−H, figures of structure directing agents, stacking sequence for layers α and α′, stacking of layers α and β and vectors $\mathbf{R}_{ij}$, effect of faulting on the X-ray powder diffraction pattern of polymorphs A, C, E, and G, XRD patterns of intergrowths of polymorphs A and C, schematic of different polymorphs obtained as a function of x and y, XRD pattern of intergrowths of layers α, α′, β, and β', and comparison of XRD pattern of SSZ-31 with the XRD pattern of the intergrowths of layers α, α′, β, and β', and input data files for DIFFaX for intergrowths of layers α, α′, β, and β' and γ, γ', δ, and δ' (40 pages). See any current masthead page for ordering and Internet access instructions.

JA963925G